LASER LIGHTCRAFT PERFORMANCE

Final Technical Report

Contract Number: H-30951D

Prepared for

National Aeronautics and Space Administration
George C. Marshall Space Flight Center
Marshall Space Flight Center, AL 35812

by

Yen-Sen Chen and Jiwen Liu

Engineering Sciences, Inc.
1900 Golf Road, Suite D
Huntsville, AL 35802
(256) 883-6233

March 2, 2000

PROJECT SUMMARY

The purpose of this study is to establish the technical ground for modeling the physics of laser powered pulse detonation phenomenon. The principle of the laser power propulsion is that when high-powered laser is focused at a small area near the surface of a thruster, the intense energy causes the electrical breakdown of the working fluid (e.g. air) and forming high speed plasma (known as the inverse Bremsstrahlung, IB, effect). The intense heat and high pressure created in the plasma consequently causes the surrounding to heat up and expand until the thrust producing shock waves are formed. This complex process of gas ionization, increase in radiation absorption and the forming of plasma and shock waves are investigated in the development of the present numerical model. In the first phase of this study, laser light focusing, radiation absorption and shock wave propagation during the laser pulsed cycle are modeled. The model geometry and test conditions of known benchmark experiments such as those in Myrabo's experiment are employed in the numerical model benchmark validation studies. The calculated performance data (e.g. coupling coefficients) are compared to the measured data. The final goal of this project is that a design tool will be available for the analysis and optimization of full-scale laser propelled flight vehicles.

1. METHOD OF APPROACH -- A BUILDING BLOCK APPROACH

An efficient design of laser propelled vehicles requires the detailed understanding of how the detonation waves behave with different thrust cavity geometry and flight conditions and the performance of the air intake configurations and arrangements. CFD methods with high-temperature thermodynamics and transient detonation wave capturing capabilities are very useful in providing information for the optimization of the laser lightcraft configurations. Compared to the other propulsion systems, modeling of laser propelled vehicles is very difficult because it involves many complicated physical phenomena such as optical breakdown, laser absorption, thermochemical and raidiative nonequilibrium, plasma dynamics, etc. The general approach of the present numerical model can be summarized in the following items:

- Computational fluid dynamics method with time accurate integration schemes and high-temperature gas thermodynamics properties
- Unstructured-mesh flow code for detonation wave prediction
- Thermal non-equilibrium energy equations monitoring the translational and vibrational states
- Modeling of the electron temperature transport and energy transfer
- Plasma ignition model to start the laser absorption
- Air breakdown/ionization chemistry model
- Specular ray tracing method for laser light reflection and focusing
- Modified discrete transfer radiation model for laser absorption and the inverse Bremsstrahlung effect
- Laser light energy absorption model
- Beam propagation and gasdynamics coupling
- Effects of air plasma non-equilibrium thermal radiation model
- Thrust integration in time for coupling coefficient calculations

2. COMPUTATIONAL FLUID DYNAMICS MODEL

The current computational model is developed based on an unstructured computational fluid dynamics (CFD) model, the UNIC-UNS code developed at Engineering Sciences, Inc., and a ray tracing radiation model for laser light reflection, focusing and absorption modeling. The underlying CFD flow solver is a general unified (all speed) solution method employed to solve the Navier-Stokes equations (Ref. 1). New models involved in this project include:

(1) high-temperature thermal dynamics properties based on the latest database released in Ref. 2;

(2) an electron temperature equation with elastic collision energy transfer described in Ref. 3;

(3) a finite-rate air chemistry model of Park (Ref. 4);

(4) a laser ray tracing model with discrete transfer method in solving the radiative transfer equation;

(5) the plasma radiation model using the LORAN code (Ref. 5); and

(6) a spark ignition model to start the laser light absorption process and chemical reactions.

2.1 Governing Equations

The continuity, Navier-Stokes, energy (total enthalpy) and electron temperature equations, can be written in a Cartesian tensor form:

$$\frac{\partial \rho}{\partial t}+\frac{\partial}{\partial x_j}\left(\rho u_j\right)=0 \tag{1}$$

$$\frac{\partial \rho u_i}{\partial t}+\frac{\partial}{\partial x_j}\left(\rho u_j u_i\right)=-\frac{\partial p}{\partial x_i}+\frac{\partial \tau_{ij}}{\partial x_j} \tag{2}$$

$$\frac{\partial \rho H}{\partial t}+\frac{\partial}{\partial x_j}\left(\rho u_j H\right)=\frac{\partial p}{\partial t}+Q_e+\frac{\partial}{\partial x_j}\left(\frac{\mu}{P_r}\nabla H\right)+\frac{\partial}{\partial x_j}\left(\left(1-\frac{\mu}{P_r}\right)\nabla\left(V^2/2\right)\right) \tag{3}$$

$$\frac{\partial}{\partial t}\left(\frac{2}{3}k_b n_e T_e\right)+\frac{\partial}{\partial x_j}\left(\frac{2}{3}k_b n_e T_e\, u_j\right)=\frac{\partial}{\partial x_j}\left(\lambda_e \frac{\partial T_e}{\partial x_j}\right)+Q_r-Q_{ec} \tag{4}$$

where ρ is the fluid density, u_i is the i^{th} Cartesian component of the velocity, p is the static pressure, μ is the fluid viscosity, P_r is the Prandtl number, H is the gas total enthalpy and V stands for the sum of velocity squared. In Eq. (4), k_b, n_e, T_e, λ_e, Q_r and Q_{ec} are the Boltzmann's constant, electron number density, electron temperature, electron thermal conductivity, radiative heat source from laser absorption and radiative transfer, and the energy transfer due to eletron/particle elastic collisions, respectively. The shear stress τ_{ij} can be expressed as:

$$\tau_{ij}=\mu\left(\frac{\partial u_i}{\partial x_j}+\frac{\partial u_j}{\partial x_i}-\frac{2}{3}\frac{\partial u_k}{\partial x_k}\delta_{ij}\right)-\frac{2}{3}\rho k\delta_{ij}$$

The species conservation equation is expressed as:

$$\frac{\partial \rho Y_i}{\partial t}+\frac{\partial}{\partial x_j}\left(\rho u_j Y_i\right)=\frac{\partial}{\partial x_j}\left[\left(\rho D\right)\frac{\partial Y_i}{\partial x_j}\right]+\dot{\omega}_i$$

where Y_i is the i^{th} species mass fraction, D is the mass diffusivity, which can be written as viscosity divided by the Schmidt number, σ_Y, and $\dot{\omega}_i$ is the chemical reaction rate for species i respectively.

2.2 Thermal Non-Equilibrium Energy Equations

For high temperature gas flows, thermal non-equilibrium state may be important. In Landau and Teller's derivation, a master equation is employed to describe the evolution of the population of quantum level N_i. This master equation is written as:

$$\frac{dN_i}{dt}=N\sum_{j=0}^{I_{\max}}K_{j\Rightarrow i}N_j-N\sum_{j=0}^{I_{\max}}K_{i\Rightarrow j}N_i;\quad i=0,1,2,\ldots,I_{\max}$$

Results from the quantum mechanical solution of the harmonic oscillator are used to relate the various quantum transition rates to one another, and then the master equation may be summed over all quantum states to arrive at the Landau-Teller equation:

$$\frac{D\rho e_v}{Dt} = \frac{\partial}{\partial x_i}\left(k_v \frac{\partial T_v}{\partial x_i}\right) + \rho \frac{e_v^{eq}(T_t) - e_v}{\tau_{LT}}$$

where ρ, e_v, e_v^{eq} and τ_{LT} represent the gas density, vibrational energy, effective (equilibrium) vibrational energy and the vibrational-translational relaxation time scale respectively. An empirical expression (to be discussed in the next section) is used to model the Landau-Teller relaxation time scale.

To solve this vibrational energy equation, a new subroutine is created to calculate the matrix coefficients (the left-hand-side of the equation) of the transport equation and the source term (the right-hand-side of the equation). The source term is further linearized to result in an explicit term and an implicit term. This treatment is important for an unconditionally stable solution of the equation. That is,

$$\text{Explicit source term} = \rho \frac{e_v^{eq}(T_t)}{\tau_{LT}}$$

$$\text{Implicit source term} = -\frac{\rho}{\tau_{LT}} e_v$$

The vibrational to translational energy transfer is computed by adding the diffusion term of the vibrational energy equation,

$$\frac{\partial}{\partial x_i}\left(k_v \frac{\partial T_v}{\partial x_i}\right)$$

to the right-hand-side of the translational energy equation as a source term.

2.3 Numerical Scheme

The cell-centered scheme is employed that the volume surfaces are represented by the grid cell surfaces. The transport equations can be written in integral form as:

$$\frac{\partial}{\partial t}\int_{\Omega} \rho\phi \, d\Omega + \oint_{\Gamma} \vec{F}\cdot\vec{n}\, d\Gamma = \oint_{\Omega} S_{\phi}\, d\Omega$$

where Ω is the domain of interest and Γ denotes the surrounding surfaces; $\vec{n}$ is a unit normal vector of Γ in the outward direction. The flux function $\vec{F}$ contains the inviscid and the viscous flux vectors,

$$\vec{F} = \rho\vec{V}\phi - \mu_{\phi}\nabla\phi$$

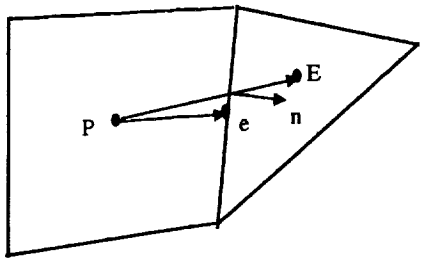

Figure 1. Unstructured control volume.

For the face *e* between control volumes *P* and *E*, the diffusive flux can be approximated as:

$$\left(\nabla\phi\bullet\vec{n}\right)_e \approx \frac{\phi_E-\phi_P}{\left|\vec{r}_E-\vec{r}_P\right|} + \overline{\nabla\phi}_e \bullet \left(\vec{n} - \frac{\vec{r}_E-\vec{r}_P}{\left|\vec{r}_E-\vec{r}_P\right|}\right)$$

And,

$$\phi_E - \phi_P \approx \overline{\nabla\phi}_e \bullet \left(\vec{r}_E - \vec{r}_P\right)$$

where $\overline{\nabla\phi}_e$ is interpolated from the neighbor cells *E* and *P*.

The finite volume formulation of flux integral can be evaluated by the summation of the flux vectors over each face,

$$\oint_{\Gamma} \vec{F} \cdot \vec{n}\, d\Gamma = \sum_{j=k(i)} F_{i,j}\, \Delta\Gamma_j$$

where k(i) is a list of faces of cell i, $F_{i,j}$ represents convection and diffusion fluxes through the interface between cell i and j, and $\Delta\Gamma_j$ is the cell-face area.

The convective flux is evaluated through the upwind-cell quantity by a linear reconstruction procedure to achieve second order accuracy:

$$\phi_e = \phi_u + \psi_e \nabla\phi_u \bullet (\vec{r}_e - \vec{r}_u)$$

where the subscript u represents the upwind cell and ψ_e is a limiter used to ensure that the reconstruction does not introduce local extrema. The limiter proposed by Barth is used here. Defining $\phi_{max} = max(\phi_u, \phi_j)$, $\phi_{min} = min(\phi_u, \phi_j)$ (and assuming ϕ_e^0 is computed with ψ_e=1) the scalar ψ_e associated with the gradient at cell u due to edge e is:

$$\psi_e = \begin{cases} min\left(1, \dfrac{\phi_{max} - \phi_u}{\phi_e^0 - \phi_u}\right) & if\ \phi_e^0 - \phi > 0 \\ min\left(1, \dfrac{\phi_{min} - \phi_u}{\phi_e^0 - \phi_u}\right) & if\ \phi_e^0 - \phi < 0 \\ 1 & if\ \phi_e^0 - \phi = 0 \end{cases}$$

2.4 Solution Procedures

A general implicit discretized time-marching scheme for the transport equations can be written as below,

$$\left(\frac{\rho^n}{\Delta t}+A_p\right)\phi_p^{n+1}=\sum_{m=1}^{NB}A_m\phi_m^{n+1}+\frac{(\rho\phi_p)^n}{\Delta t}+S_\phi$$

where *NB* means the neighbor cells of cell P. The high order differencing term and cross diffusion term are treated using known quantities and retained in the source term and updated explicitly.

A predictor/corrector solution algorithm is employed to provide coupling of the governing equations.

The discretized finite-volume equations form a set of linear algebra equations, which are non-symmetric matrix system with arbitrary sparsity patterns. The preconditioned Bi-CGSTAB and GMRES(*m*) matrix solvers are used to efficiently solve the linear algebra equations.

2.5 Finite-Rate Chemistry Model

For gas-phase chemical reaction modeling, a general system of chemical reactions can be written in terms of its stoichiometric coefficients (ν_{ij} and ν_{ij}') and the i^{th} chemical species name (M_i) of the j^{th} reaction as

$$\sum_i \upsilon_{ij} M_i = \sum_i \upsilon_{ij}' M_i$$

The net rate of change in the molar concentration of species *i* due to reactions *j*, X_{ij}, and the species production rate can be written as:

$$X_{ij}=\left(\upsilon_{ij}'-\upsilon_{ij}\right)\left[K_{fj}\prod_i\left(\frac{\rho Y_i}{M_{Wi}}\right)^{\upsilon_{ij}}-K_{bj}\prod_i\left(\frac{\rho Y_i}{M_{Wi}}\right)^{\upsilon_{ij}'}\right]$$

$$\dot{\omega}_i = Mw_i\sum_j X_{ij}$$

The forward (Arrhenius law) and backward reaction rates for each reaction is given by:

$$Kf_j = A_j T^{B_j} Exp(-\frac{E_j}{RT})$$

$$Kb_j = \frac{Kf_j}{Ke_j}$$

where Ke_j is the equilibrium coefficient

$$Ke_j = (RT)^{-\sum_{i=1}^{n}(\nu'_{ij}-\nu_{ij})} Exp\left[-\frac{\sum_{i=1}^{n}(\nu'_{ij}-\nu_{ij})\,g_i}{RT}\right]$$

A point-implicit (operator splitting) method is employed to solve the chemistry system.

2.6 Air Chemistry Model

The air chemical kinetics model of Park (Ref. 4) is employed in the present study. This model is listed in Table 1. The light emission effects due to the radiative recombination reactions, in the last two reactions, are not modeled in the current study. This effect will be investigated in future study. Other chemistry models such as the one described in Ref. 6 were also tested. That model, however, caused very high stiffness in the high electron temperature regime. It is therefore not selected for the final model. The current chemistry model involves 11 species and 51 reactions. The present point implicit finite-rate method have is very robust in providing solutions of this system.

Table 1. Air Chemistry Model

REACT RATE: K = A*T**(+N)*EXP(-E/RT)

I	A	N	E/R	Temperature(T)	(EQUATIONS)
1	7.0000e21	-1.60	113200.0	Tc	N2 + N2 = 2 N + N2
2	7.0000e21	-1.60	113200.0	Tc	N2 + O2 = 2 N + O2
3	7.0000e21	-1.60	113200.0	Tc	N2 + NO = 2 N + NO
4	7.0000e21	-1.60	113200.0	Tc	N2 + NO+ = 2 N + NO+
5	3.0000e22	-1.60	113200.0	Tc	N2 + N = 2 N + N
6	3.0000e22	-1.60	113200.0	Tc	N2 + N+ = 2 N + N+
7	3.0000e22	-1.60	113200.0	Tc	N2 + O = 2 N + O
8	3.0000e22	-1.60	113200.0	Tc	N2 + O+ = 2 N + O+
9	7.0000e21	-1.60	113200.0	Tc	N2 + N2+ = 2 N + N2+
10	7.0000e21	-1.60	113200.0	Tc	N2 + O2+ = 2 N + O2+
11	1.2000e25	-1.60	113200.0	Tc	N2 + E = 2 N + E
12	2.0000e21	-1.50	59500.0	Tc	O2 + N2 = 2 O + N2
13	2.0000e21	-1.50	59500.0	Tc	O2 + O2 = 2 O + O2
14	2.0000e21	-1.50	59500.0	Tc	O2 + NO = 2 O + NO
15	2.0000e21	-1.50	59500.0	Tc	O2 + NO+ = 2 O+ NO+
16	1.0000e22	-1.50	59500.0	Tc	O2 + N = 2 O + N
17	1.0000e22	-1.50	59500.0	Tc	O2 + N+ = 2 O + N+
18	1.0000e22	-1.50	59500.0	Tc	O2 + O = 2 O + O
19	1.0000e22	-1.50	59500.0	Tc	O2 + O+ = 2 O + O+
20	2.0000e21	-1.50	59500.0	Tc	O2 + N2+ = 2 O + N2+
21	2.0000e21	-1.50	59500.0	Tc	O2 + O2+ = 2 O + O2+
22	5.0000e15	0.00	75500.0	Tc	NO + N2 = N + O + N2
23	5.0000e15	0.00	75500.0	Tc	NO + O2 = N + O + O2
24	1.1000e17	0.00	75500.0	Tc	NO + NO = N + O + NO
25	5.0000e15	0.00	75500.0	Tc	NO + NO+ = N + O + NO+
26	1.1000e17	0.00	75500.0	Tc	NO + N = N + O + N
27	1.1000e17	0.00	75500.0	Tc	NO + N+ = N + O+ N+
28	1.1000e17	0.00	75500.0	Tc	NO + O = N + O + O
29	1.1000e17	0.00	75500.0	Tc	NO + O+ = N + O + O+
30	5.0000e15	0.00	75500.0	Tc	NO + N2+ = N + O + N2+
31	5.0000e15	0.00	75500.0	Tc	NO + O2+ = N + O + O2+
32	8.4000e12	0.00	19400.0	Tg	NO + O = O2 + N
33	6.4000e17	-1.00	38400.0	Tg	N2 + O = NO + N
34	8.8000e08	1.00	31900.0	Tg	N + O = NO+ + E
35	7.1000e02	2.70	80600.0	Tg	2 O = O2+ + E
36	4.4000e07	1.50	67500.0	Tg	2 N = N2+ + E
37	1.0000e12	0.50	77200.0	Tg	NO+ + O = N+ + O2
38	1.0000e12	0.50	12200.0	Tg	N+ + N2 = N2+ + N
39	8.7000e13	0.14	28600.0	Tg	O2+ + N = N+ + O2
40	1.4000e05	1.90	26600.0	Tg	NO + O+ = N+ + O2
41	9.9000e12	0.00	40700.0	Tg	O2+ + N2 = N2+ + O2
42	4.0000e12	-0.09	18000.0	Tg	O2+ + O = O+ + O2
43	3.4000e13	-1.08	12800.0	Tg	NO+ + N = N2 + O+
44	2.4000e13	0.41	32600.0	Tg	NO+ + O2 = O2+ + NO
45	7.2000e12	0.29	48600.0	Tg	NO+ + O = O2+ + N
46	9.1000e11	0.36	22800.0	Tg	O+ + N2 = N2+ + O
47	7.2000e13	0.00	35500.0	Tg	NO+ + N = O + N2+
48	3.9000e33	-3.78	158500.0	Te	O + E = O+ + E + E
49	2.5000e34	-3.82	168600.0	Te	N + E = N+ + E + E
50	1.0700e11	-0.52	0.0	Te	O+ + E + E = O + E
51	1.5200e11	-0.48	0.0	Te	N+ + E + E = N + E

where Tg stands for the gas temperature, Te is the electron temperature and Tc denotes the geometric averaged temperature, i.e. $T_c = \sqrt{T_g T_v}$. T_v is the vibrational temperature.

3. RADIATIVE HEAT TRANSFER MODEL

3.1 Advantages and Disadvantages of Discrete Transfer Method

The discrete ordinate method (DOM) and discrete transfer method (DTM) are currently two of the most widely used methods for modeling radiation in participating media, and they have many similarities. In both of these two methods, the radiative transfer equation (RTE) is solved only along discrete directions that approximate angular intensity distributions. As a result, they are mathematically very simple and relatively easy to code; they are able to treat multi-dimensional problems with complicated geometries (including shadowing effects) with ease; they can account for spectral effects from gases or surfaces; they are compatible with numerical algorithms for solving other transport equations. The difference between the DOM and DTM lies in how the RTE is solved. The former uses the finite difference method to solve the RTE while the latter uses the ray tracing method to solve the RTE.

During the pulsed laser plasma ignition process the major quantity of interest from laser radiation is the net radiative heat transfer along the laser beam, q_r, and it enters the governing equations through the energy source term. The wavelength dependent expression for q_r is given by

$$q_r = \sum_{k=1}^{N_b} (\alpha_k G_k - \varepsilon_k E_{bk}) \tag{5}$$

where the subscript k refers to a particular radiation band and N_b designates the total number of bands used in describing the wavelength dependence of the absorptivity α and emissivity ε; G denotes the incident radiation on the surface; E_b represents the radiative emissive power defined by the Planck function. In the DOM and DTM, the quantity G can be further expressed as

$$G = \sum_{k=1}^{N_b} G_k = \sum_{k=1}^{N_b} \sum_{n\cdot\Omega_m<0}^{m=1,M} G_{km} = \sum_{k=1}^{N_b} \sum_{n\cdot\Omega_m<0}^{m=1,M} I_{km}\Delta\omega_m \quad (6)$$

where n represents the unit normal vector on the wall; Ω_m refers to the m-th specific discrete direction; $\Delta\omega_m$ is the corresponding solid angle for the m-th discrete direction; G_{km}, I_{km} represent the incident radiation and incident intensity along the m-th direction at the k-th band, respectively. The DOM is not suitable for modeling surface radiation because it has to model radiation transport through each gas control volume even though the gas is not radiatively participating, and it is subsequently expensive. The DTM has been also rarely used to model surface radiation solely due to its fundamental shortcoming, the ray effects.

To illustrate the ray effects in DTM, consider a radiation incident on a surface cell on the bottom wall over a control angle for a 3D box as shown in Fig. 6. The center point of the incident surface cell is O. The control angle is intercepted by the top wall and the intercepted area is represented by the shadowed area ABCD. Each surface of the box is divided into many small surface cells, the area ABCD thus consists of several surface cells. Some cells are entirely located inside the ABCD while others are partially located in the ABCD. The temperature and radiative properties on each cell may be different from others. In the traditional approach of the DTM, radiation contribution from the area ABCD to the incident surface cell is assumed to come from only a single surface cell, for example, where the point P is located in Fig. 2. Unless a large amount of discrete directions are chosen, this treatment neglects the contribution from other surface cells, thus leads to a poor accuracy in the results. This is so called the ray effects. The ray effects also exist in the gas radiation modeling but they become less prominent due to the mitigation of gas radiation.

3.2 Modified Discrete Transfer Method

In order to eliminate the ray effects, the traditional DTM is modified by considering radiation contribution from all surface cells in the ABCD. Thus Eq. (6) becomes,

$$G = \sum_{k=1}^{N_b} \sum_{n\cdot\Omega_m<0}^{m=1,M} \sum_{j=1}^{N} I_{kmj} \Delta\omega_{mj} \tag{7}$$

where j refers to the j-th surface cell in the ABCD; I_{kmj} is the radiative intensity from the j-th cell along the m-th direction at the k-th band, and $\Delta\omega_{mj}$ is the solid angle with which the point O is seen by the j-th surface cell. The modified DTM (MDTM) keeps all the advantages of DTM such as easy consideration of spectral, specular, shadowing effects, easy coding and easy coupling with other transport equations while it provides a high accuracy in the results. Calculation of $\Delta\omega_{mj}$ requires an evaluation of all surface cell areas intercepted by a control angle on the wall, and subsequently the ray tracing time is increased compared to the DTM. However, this increase is of minor effects since the surface cell number only takes a small percentage of the total cell number and $\Delta\omega_{mj}$ is evaluated only once in the transient simulation of practical systems. Extension of the MDTM to the gas radiation problems requires a significant increase of ray tracing calculation, thus is not encouraged.

The dependent variable in the MDTM is the radiative intensity as seen in Eqs. (6) and (7) and its value is initially not known. Thus, an iterative solution procedure is required in the above modeling of surface radiation. That is, an initial intensity solution is assumed and it is used to calculate the incident radiation G, then the incident radiation G and the Planck function are applied on the radiative boundary condition to obtain the new intensity solution. With new intensity solution, the new incident radiation can be calculated again. This iterative procedure continues until the maximum difference in the incident

radiation between two consecutive iterations is less than a designated tolerance. For a diffuse wall, the radiative boundary condition is given as

$$I_{km} = \varepsilon_k \frac{E_{bk}}{\pi} + \frac{(1-\varepsilon_k)}{\pi} \sum_{n\cdot\Omega_{m'}<0}^{m'=1,M} G_{km'} \tag{8}$$

For a specular wall, the radiative boundary condition becomes

$$I_{km} = \varepsilon_k \frac{E_{bk}}{\pi} + \frac{(1-\varepsilon_k)}{\pi} G_{km'} \tag{9}$$

In Eq. (8), the all arriving intensities have a contribution to the calculation of I_{km} while in Eq. (9), only one arriving intensity, whose direction is aligned with the mirror direction of the m-th direction, has a contribution to the calculation of I_{km}.

3.3 Surface Cell Areas Intercepted by a Control Angle

As indicated previously, the major calculation in the implementation of the MDTM comes from the evaluation of the solid angles with which surface cells partially or entirely intercepted by a control angle are seen from a certain point. Considering that a solid angle is defined as the projection of the surface onto a plane normal to the direction vector, divided by the distance squared, the major calculation in the MDTM thus becomes the calculation of surface cell areas. For some surface cells, entire area must be calculated while for others only portion of area need to be calculated as seen in Fig. 2. The following paragraphs will discuss how the surface cell areas are evaluated in this study.

The first step is to select an appropriate discretization strategy for the angular domain. Due to its easy division and wide applications, the azimuthal discretization strategy as shown in Fig. 3 is chosen in this study. In this strategy, the 4π angular domain at a volume cell is divided into a finite number of discrete,

nonoverlapping solid angles along the azimuthal and polar directions. The angle increments along these two directions are usually uniform. For a surface radiation problem, only surface cells are taken into account and their angular domain is half of that for a volume cell. In Fig. 3, the shadowed area represents the projection of a control angle on a hemisphere of unit radius and it contains four vertex points. In this study, the direction vectors that connect the point O on the surface and four vertex points are called the vertex vector. A ray travelling along a vertex vector is called the vertex ray. Four vertex rays uniquely decide a control angle.

The second step is to find the intersection points between the four vertex rays from a control angle and a wall as shown as the points A, B, C and D in Fig. 2. For the simulation in manufacturing and materials processing, the gas region usually needs to be discretized due to the involvement of other transport phenomena. With discretization of the gas region, calculation of the intersection point between a vertex ray and a wall becomes easy and straightforward. A vertex ray emitted from a surface cell is just traced through the adjacent volume cells until it is intercepted by a wall. Such a ray tracing calculation is very efficient and accurate.

The third step is to determine the penetrating points of all surface cell edges passing through the four planes as shown in Fig. 2 as OAB, OAD, ODC, and OBC that form a control angle. These planes are defined by the two adjacent vertex vectors and limited between the corresponding vertex rays. Calculation of this step starts from one of the intersection points between the vertex rays and a wall, for example, the point A. The surface cell index number where the point A is located must be found at first. Then, each edge of this cell is examined to see if it penetrates any of four planes forming the given control angle. If one of these edges is found, the penetrating point must be determined. After that, the search goes to the adjacent surface cell with the common edge. This procedure continues until all the penetrating points are found.

The fourth step is to determine the vertexes of surface cells which are located inside the specified control angle. This step starts from a surface cell which has at least an edge penetrating one of the four planes forming the control angel. Each vertex of this cell is examined to see if it is located inside the control angle. If one of these vertexes is found, it is then saved and the search moves to the adjacent cells with the common vertex. This procedure repeats until a surface cell is found which has no vertex located inside the control angle.

The fifth step is to calculate the areas of the surface cells contained inside the control angle. In this step, all penetrating points determined in Step (3) and vertexes determined in Step (4) are sorted and regrouped. Those points which are attached to the same surface cell are put together, and the area of the polygon formed by these points can then determined easily.

In the above five steps, the Step (3) is the most computationally extensive. This is especially true for a 2D axisymmetric geometry. In such a case, the edges of a surface cell may be no longer straight lines as in 2D planar and 3D geometries. Thus, much more calculation has to be involved to find a valid penetrating point. Development of an accurate and efficient method for calculating the surface cell areas intercepted by the control angles represents one of the most important tasks in the implementation of the MDTM. The above method for calculating the surface cell areas has a room for improvement by using some advanced ray tracing techniques developed in computer graphics.

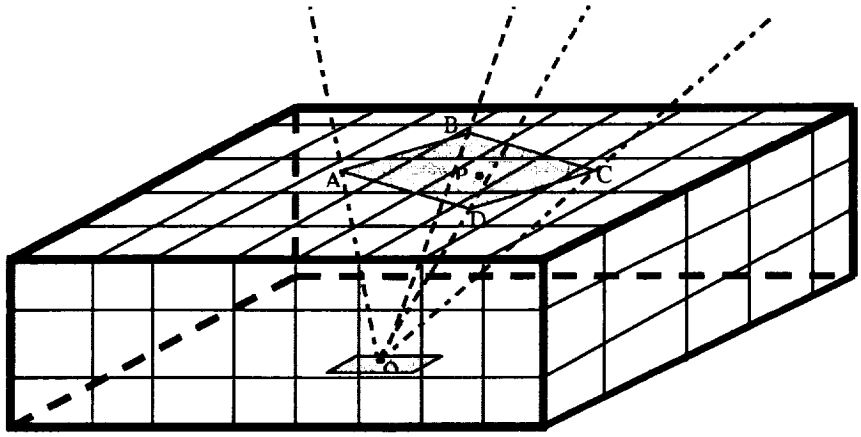

Figure 2. Concept for the modified discrete transfer method

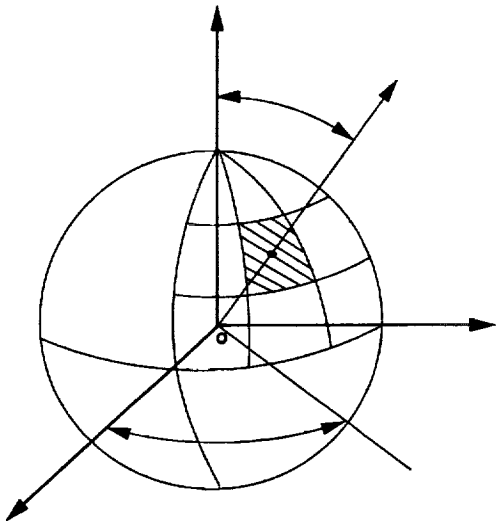

Figure 3. Azimuthal discretization strategy

4. Non-equilibrium Radiative Heat Transfer

The non-equilibrium radiation model needed for high temperature plasma is implemented based on the LORAN code of NASA Langley Research Center. The code is acquired from Langley, several published cases were tested before the implementation is started. After some adjustment of the input parameters, the code reproduced the results in the literature for high-temperature gas radiation.

Implementation and coupling of the LORAN code with UNIC-UNS/ GRASP-UNS need further investigation due to the large amount of computational effort would be needed if it is solved for every grid point. The LORAN code solves thousands of bands in the radiative transfer model. More efficient method would be required to make this model computationally feasible.

The general consideration of the non-equilibrium radiation effects and model adapted are summarized in the following. Conclusion of a preliminary study about the significance of its effects is also given below.

1. Neglecting transients and assuming a non-scattering medium, the complete radiative transfer equation (RTE) becomes

$$\frac{dI_\omega(s,\vec{\Omega})}{ds} + \kappa_\omega I_\omega(s,\vec{\Omega}) = j_\omega^e(s)$$

   where I_ω represents spectral radiation intensity, and κ_ω and j_ω^e denote the absorption coefficient and the emission coefficient, respectively.

2. In equilibrium gases, the electronic energy-level populations are determined as a function of a uniquely defined equilibrium temperature according to a Boltzmann distribution, and κ_ω and j_ω^e are related according to Kirchhoff's law as $j_\omega^e(s) = \kappa_\omega I_\omega^b(s)$, where $I_\omega^b(s)$ is blackbody intensity determined by Planck function.

In non-equilibrium flow, however, all these simple relations no longer apply and the non-equilibrium absorption and emission coefficients must be determined through the non-equilibrium populations of each energy level and transitions of various energy levels.

3. Plasma air includes the following atomic and molecular species: O, N, NO, N^+, O^+, N_2, O_2, etc. which all contribute to the non-equilibrium radiative heat transfer. To determine κ_ω and j_ω^e for these species, the following four radiative transitions must be taken into account:

   - Atomic Line Transitions
   - Atomic Bound-free Transitions
   - Atomic Free-free Transitions
   - Molecular Transitions

4. Currently, there are two codes available, which provide detailed information on these transitions. One is NEQAIR developed by Park and another is LORAN developed by Hartung. Because these codes involve large database, they are rarely applied in practical problems. To overcome disadvantage of these code, some simple models have been developed such as Park's PRG model etc.

5. With the determination of κ_ω and j_ω^e, the RTE can be solved by either deterministic or stochastic approach. Unlike the most CFD equations, RTE is integral differential equation and numerical treatment is, thus, different from CFD approach. Currently, there are several methods available for solving non-equilibrium radiative heat transfer, which include Monte Carlo method, P-1 method, S-N method, quadromoment method, etc. The Monte Carlo is accurate but too costly and time-consuming for practical applications. The P-1 and quadromoment methods are not applicable for optically thin medium. The

S-N method can provide accurate results for all optical ranges if the discrete direction number is big enough.

6. In the present project, the S-N method and the finite volume method were used in short duration test runs. It is found that the non-equilibrium radiation model is very computational intensive. It is typically more than ten times slower than the model without non-equilibrium radiation model. Also, preliminary studies have shown that its contribution to the overall energy reduction (cooling effect) is only less than 10 percent. Therefore, this model is not used in the final performance prediction runs.

4.1 Non-equilibrium Air Plasma Radiation Analysis

The current modeling efforts for radiative heat transfer in laser induced plasmas involve many assumptions. Some of these assumptions are usually not valid and thus cause considerably errors in the modeling results. In the present study, efforts have been made to employ less assumptions and more accurate methods and models. Treatment of plasma radiative heat transfer involves solving the radiative transfer equation (RTE). Neglecting transients and assuming a noscattering medium, the complete RTE becomes

$$\frac{dI_\omega(s,\vec{\Omega})}{ds} + \kappa_\omega I_\omega(s,\vec{\Omega}) = j_\omega^e(s)$$

where I_ω represents spectral radiation intensity, and κ_ω and j_ω^e denote the plasma spectral absorption coefficient and the emission coefficient, respectively.

In equilibrium gases, the electronic energy-level populations are determined as a function of a uniquely defined equilibrium temperature according to a Boltzmann distribution, and κ_ω and j_ω^e are related according to Kirchhoff's law as $j_\omega^e(s) = \kappa_\omega I_\omega^b(s)$, where $I_\omega^b(s)$ is blackbody intensity determined by Planck

function. In non-equilibrium flow, however, all these simple relations no longer apply and the non-equilibrium absorption and emission coefficients must be determined by the non-equilibrium populations of each energy level and transitions of various energy levels.

Air plasma includes following atomic and molecular species: O, N, NO, N^+, O^+, NO^+, N_2, O_2, etc. which all contribute to the non-equilibrium radiative heat transfer. To determine κ_ω and j_ω^e for these species, the following four radiative transitions must be taken into account: atomic line transitions, atomic bound-free transitions, atomic free-free transitions, and molecular transitions. Currently, there are two codes available, which provide detailed information on these transitions. One code is NEQAIR developed by Park (Ref. 7) and another LORAN developed by Hartung (Ref. 8). Because NEQAIR code involves large database, they are rarely applied in practical problems. In this study, LORAN code is used to calculate the air plasma radiative properties.

With the determination of κ_ω and j_ω^e, the RTE can be solved by either deterministic or stochastic approach. Unlike the most CFD equations, RTE is integral differential equation and numerical treatment is, thus, different from CFD approach. Currently, there are several methods available for solving non-equilibrium radiative heat transfer which include Monte Carlo method, P-1 method, quadromoment method, discrete ordinates method (DOM), discrete transfer method (DTM), etc. The Monte Carlo is accurate but too time-consuming for practical applications. The P-1 method and quadromoment method are only accurate for optically thick medium. The DOM and DTM are mathematically very simple and they can provide accurate results for all optical ranges if the discrete direction number is reasonable large. Thus, the DOM and DTM are very suitable for modeling radiation with a participating medium. For the laser propelled vehicle application, the high temperature region where non-equilibrium radiation is prominent is usually relatively small compared to the flow region considered. If the DOM is applied, RTE must be solved in the entire flow region, thus, much of

the CPU time is wasted in the regions where radiation is not important. However, with the use of the DTM, RTE can be solved in the designated region. Therefore, the DTM is selected to solve the RTE in this study due to its high efficiency in solving the RTE.

4.2 Results of Non-equilibrium Radiation Code Testing

Based on the analysis described above, a computer code has been developed which is able to simulate multi-dimensional radiative heat transfer on unstructured grids in laser induced air plasmas. Before this code was coupled into the UNIC-UNS code, the LORAN code has been tested in order to gain a confidence on its usage. The LORAN code is available from NASA Langley Research Center and it consists of over fifty subroutines. The original code was designed for coupling with 1D flow problems in a CRAY computer and its execution includes two separate steps involving spectrum setting up and radiation calculation. For the convenience of the present application, the code structure of the LORAN has been modified significantly. The modified code can be used to any UNIX computers and can be easily coupled into general CFD codes. In order to validate the accuracy of the modified LORAN code, two problems were selected and calculated absorption coefficient and/or emission coefficient were compared with available other results.

Figure 4 shows the predicted absorption coefficient and emission coefficient distributions for equilibrium air with P=2 atm and T=10,000 K. Compared to the corresponding results predicted by the original LORAN code presented in Ref. 9, solutions from two codes are essentially identical. Figure 5 shows the predicted absorption coefficient distribution for equilibrium air with P=1 atm and T=14,000 K. These results are very close to the other solutions presented on page 669 of Ref. 10. It is noted that the atomic line contributions are excluded in Figure 5 in order to create the same conditions as used in Ref. 10.

With the validation of the modified LORAN code, the radiation code developed in this study was then coupled into the UNIC-UNS code to investigate the effects of plasma radiation on the flow field. Figure 6 demonstrates the global laser absorption efficiency, temperature, pressure variations for the cases without and with consideration of plasma radiation during time 1μs to 20 μs. The temperature and pressure are presented for a specific point closed to the focal point. Comparisons of results at different cases clearly indicate that plasma radiation has important effects on the flowfield at high temperatures, especially on the temperature distribution. Therefore, accurate prediction of plasma radiation becomes essential for high temperature regions. The drawback of coupling radiation into flow solver is its tremendous CPU time. Currently, the CPU time involving radiation coupling may be orders magnitude higher than that not involving radiation coupling. So, future development of non-equilibrium radiation model must focus on the improvement of computational efficiency.

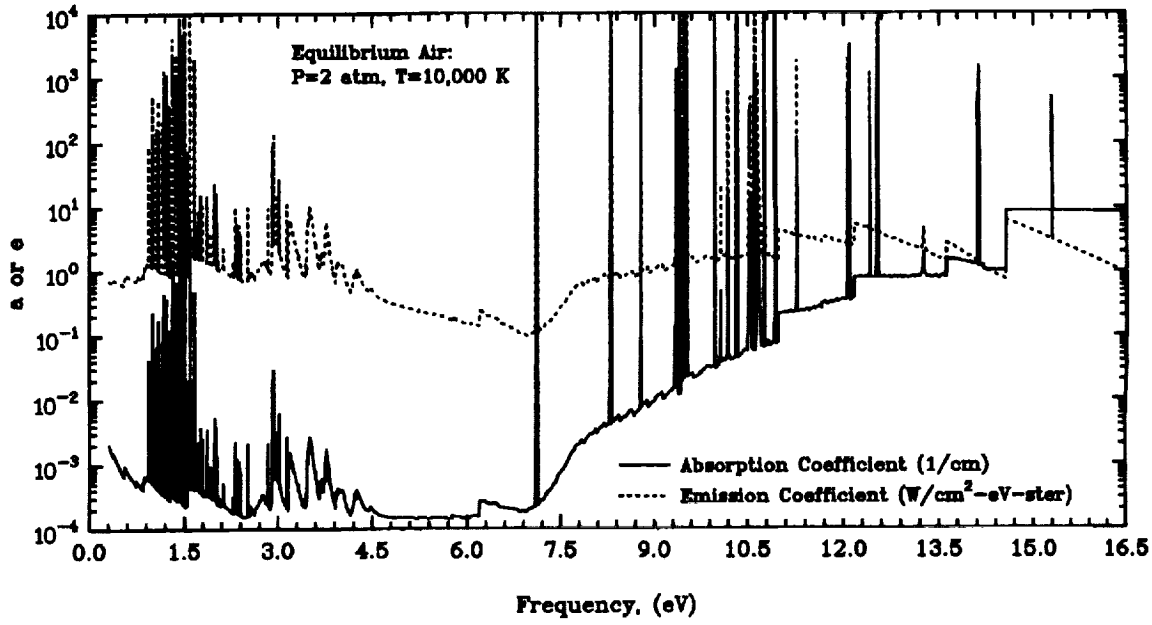

Figure 4. Absorption and emission coefficients for equilibrium air conditions.

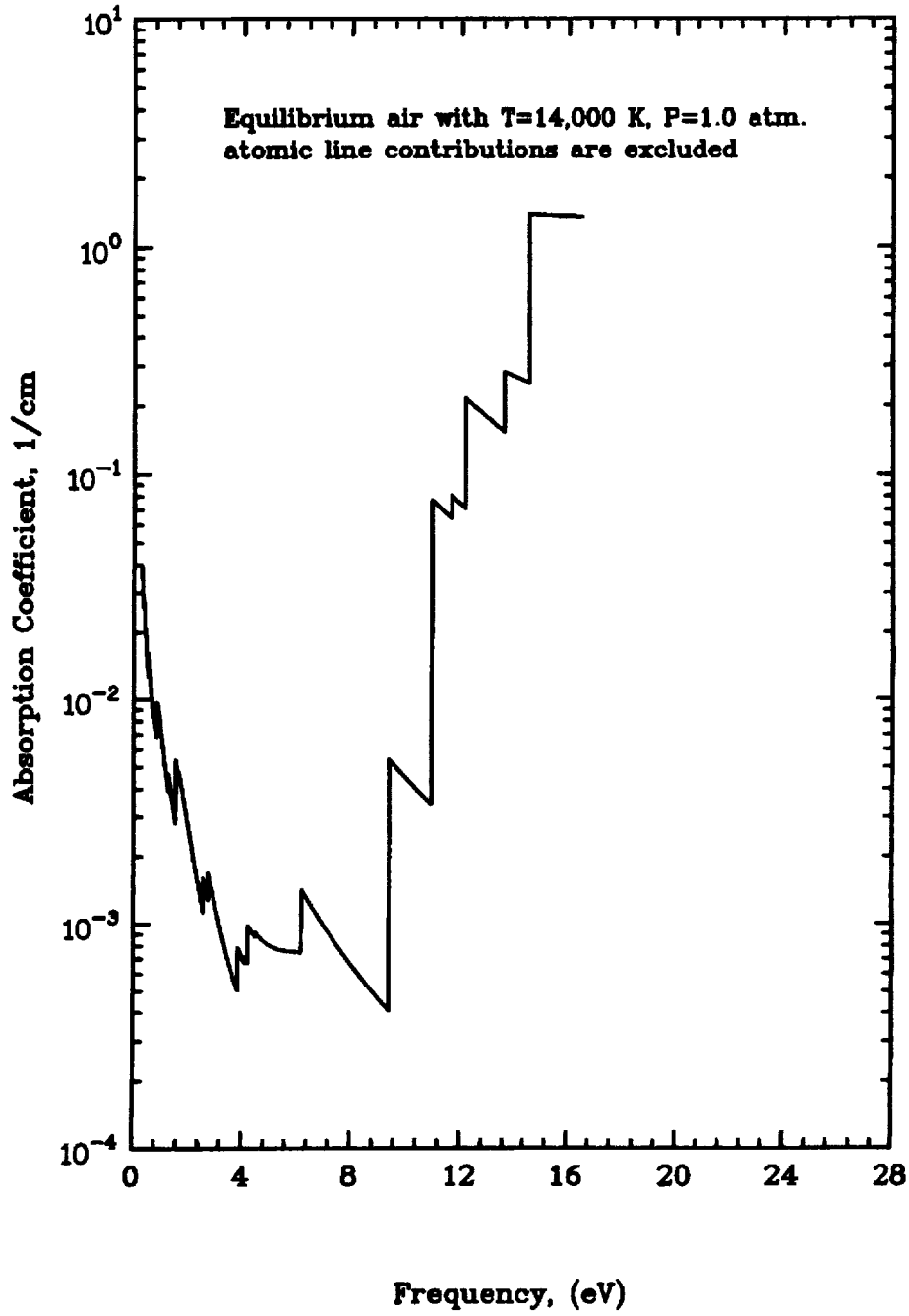

Figure 5. Absorption coefficient at equilibrium air conditions

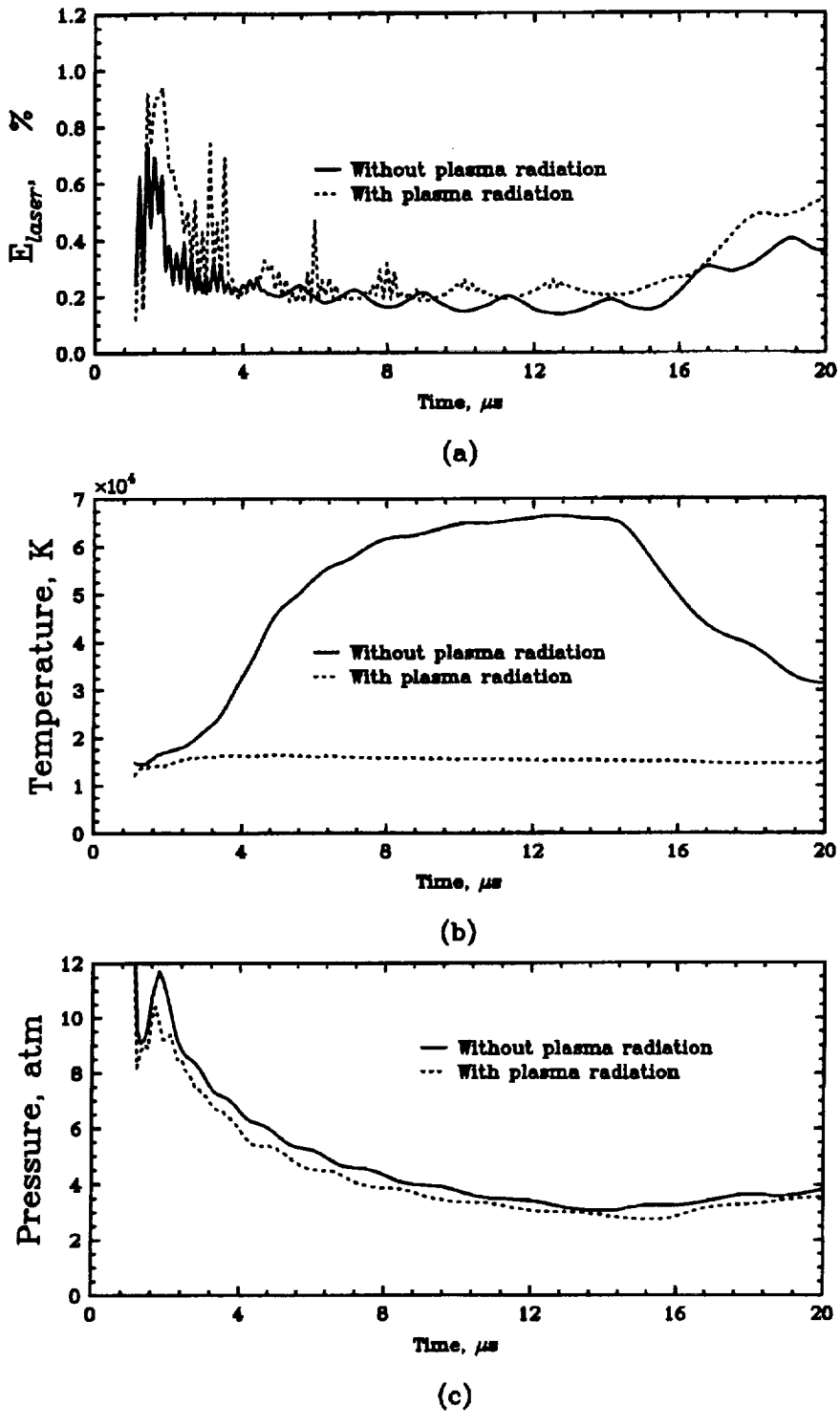

Figure 6. Effects of plasma radiation on global laser absorption coefficient, temperature, and pressure.

5. BENCHMARK TEST CASE STUDY

To demonstrate the validity and effectiveness of the numerical model developed herein in predicting the performance data of a laser light craft, three test cases with different power levels were investigated in the present study. The test conditions of these cases are listed below. The laser ray tracing testing and time-sequence flowfield solutions using the grid system below are shown in the following pages.

- Vehicle Configuration-A of Myrabo's Flight Tests (Closed Air Inlet)
- Pulsed Laser at 10 Hz and 30 μs Pulse Width
- Laser Energy Level Up To 800 J (Test Points: 400 J, 600 J and 800 J)
- Total Number of Mesh Elements = 26,318
- Assuming Axisymmetric Model
- Employs an automatic spark ignition scheme that the spark energy is switched off when the laser absorption efficiency reaches 15 percent. Also, only 15 percent of the beam power is used during the spark ignition.
- Assuming 30 percent laser absorption where electron number density (related to the plasma frequency) reaches the resonance level, i.e. 2.51372E+23/m^3.
- With Ray Tracing and Radiation Coupling
- Testing the Predictions of Detonation Wave Propagation and Vehicle Thrust Calculation

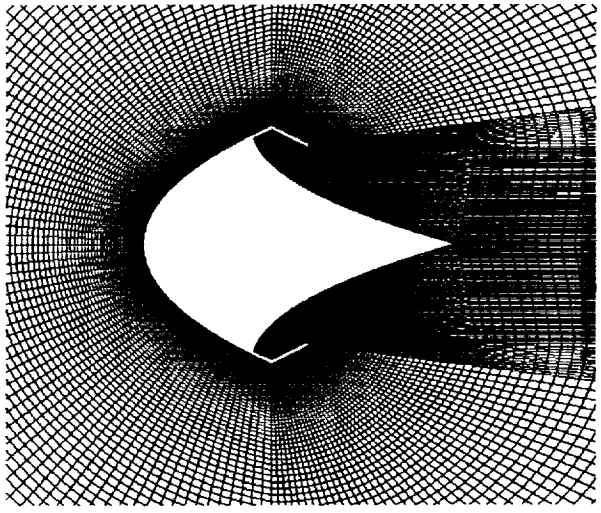

Figure 7. Mesh system used in the present laser light craft performance study.

5.1 Testing of the Ray Tracing Model

The ray-tracing model is implemented in the UNIC-UNS code to simulate the laser ray reflection and focusing effects. At first, to avoid the inaccuracy caused by possible numerical noise in the wall curvature calculation, an analytical wall contour equation is used in the model. Later, a high accuracy method is employed to recover the analytical solution accurately based on the discrete grid points. The latter approach is general and produces accurate results.

Figure 8 shows the results of ray tracing for the model-A configuration. A close up view near the focal point is shown in Figure 9. The red dots represent the ray-traced locations. The results give correct representation of the laser reflection and focusing effects.

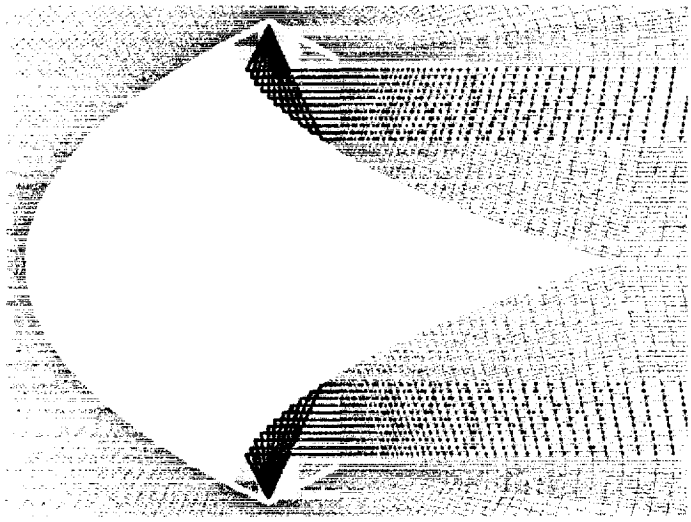

Figure 8. Model-A laser rays calculated by the ray-tracing model.

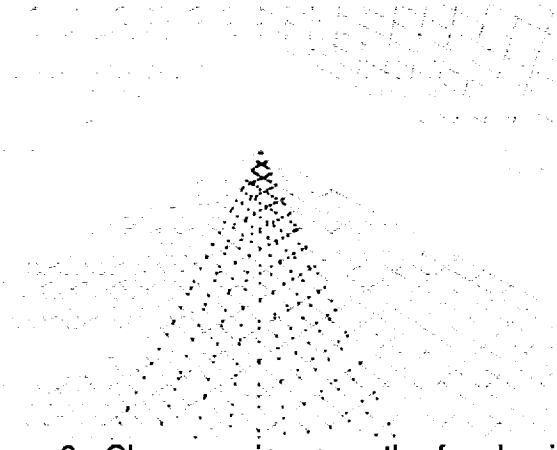

Figure 9. Close up view near the focal point.

5.2 Flowfield Solutions

The numerical computation is started with an assigned region of spark ignition near the laser focal point (a pie-shaped region covered by the beam). It is assumed that during this period, only 15 percent of the beam energy is converted to thermal energy. The spark ignition period is terminated when the laser absorption efficiency, calculated by the radiation model, researches 15 percent. At this time the maximum gas temperature reaches above 39,000 degrees K and the air plasma and a detonation wave are formed around the focal point. Local electron number density continues to grow until it reaches a level that the plasma frequency would be resonant with the laser frequency. When this level is reached, it is assumed that the laser energy is 100 percent absorbed by the electron and 30 percent of this energy is converted to thermal energy.

Three cases with laser power level of 400 Joules, 600 Joules and 800 Joules are simulated. The vehicle thrust is calculated be integrating forces along the surfaces. Integration of the thrust with time is then recorded to calculate the coupling coefficient, which is defined as:

$$\text{Coupling Coefficient} = \frac{\int (Vehicle - Thrust)dt}{Laser - Power - Input} \times 10^5, \text{ in (dynes-sec/Joules)}$$

Other data, such as cumulative spark and laser energy and temperature, pressure and electron number density ranges are also recorded for analysis. Figures 10 to 14 shows the evolution of the detonation wave in pressure contours time sequence for the 400 Joules case. Temperature and electron number density contour plots at 19 microsecond are shown in Figure 15 to 17. Figure 15 shows the case without the plasma frequency limit. In Figure 16, this limit is turned on, which shows that the laser beams are terminated at locations where the electron number density is on or above the resonance value.

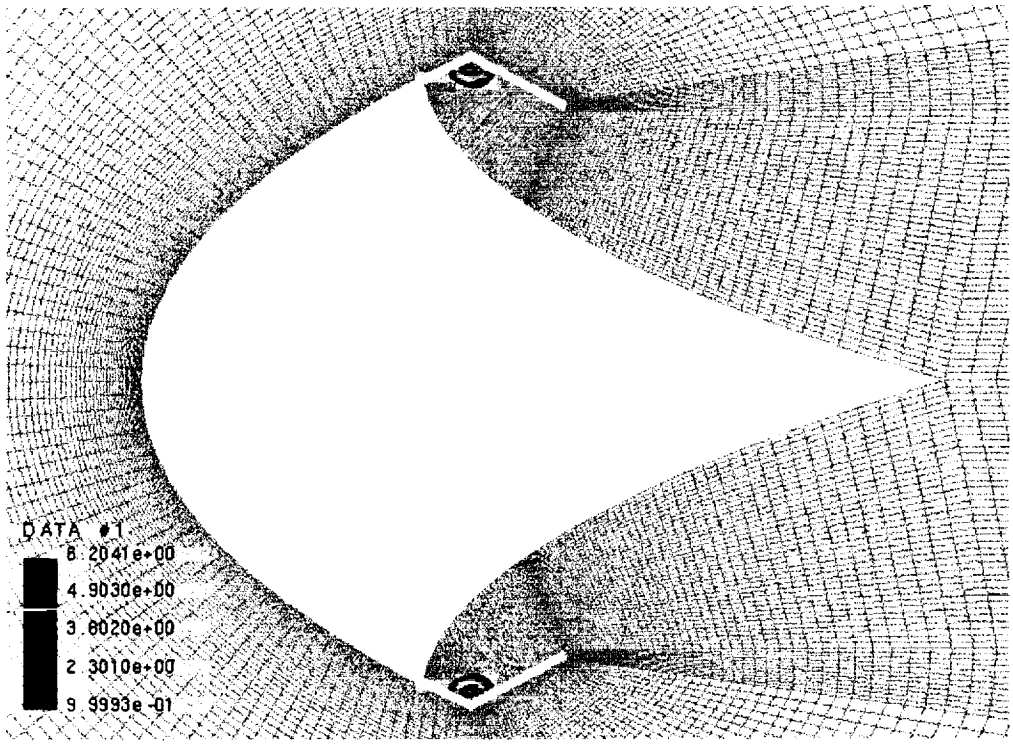

Figure 10. Pressure distributions (ATM) at 5 microseconds.

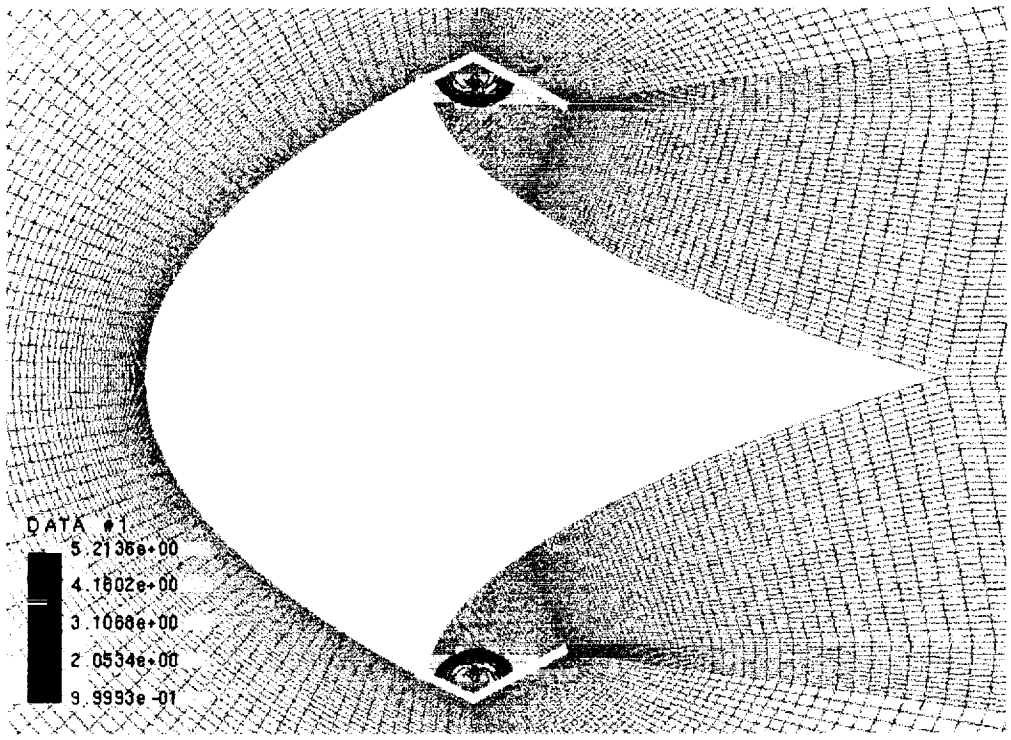

Figure 11. Pressure distributions (ATM) at 10 microseconds.

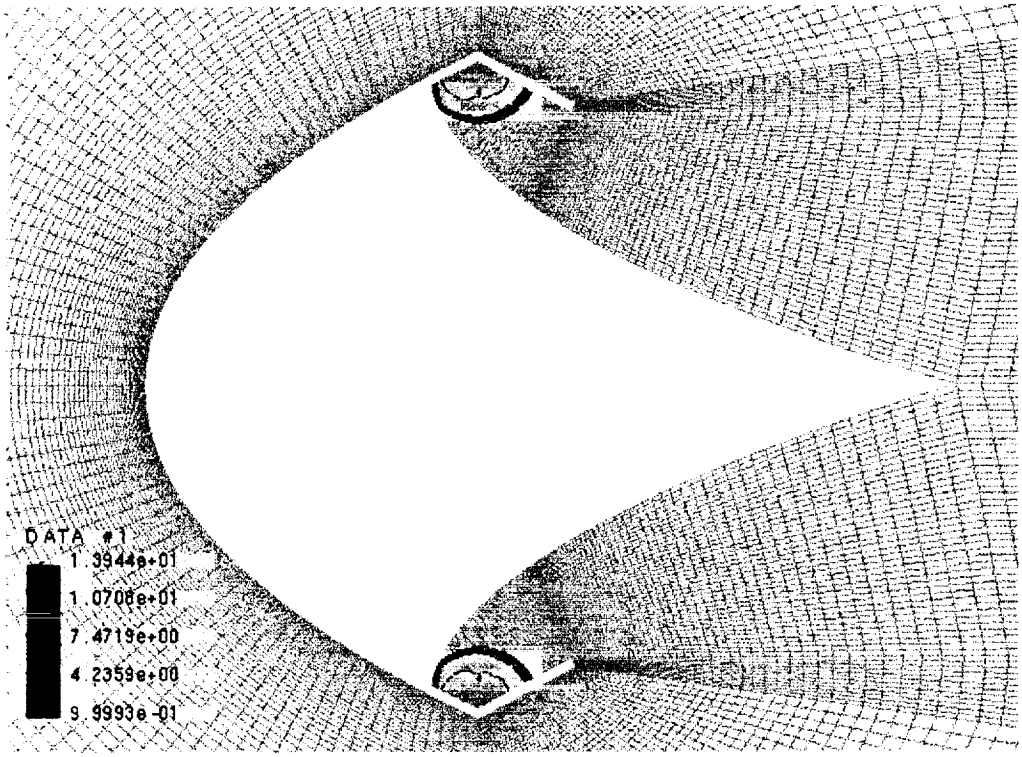

Figure 12. Pressure distributions (ATM) at 15 microseconds.

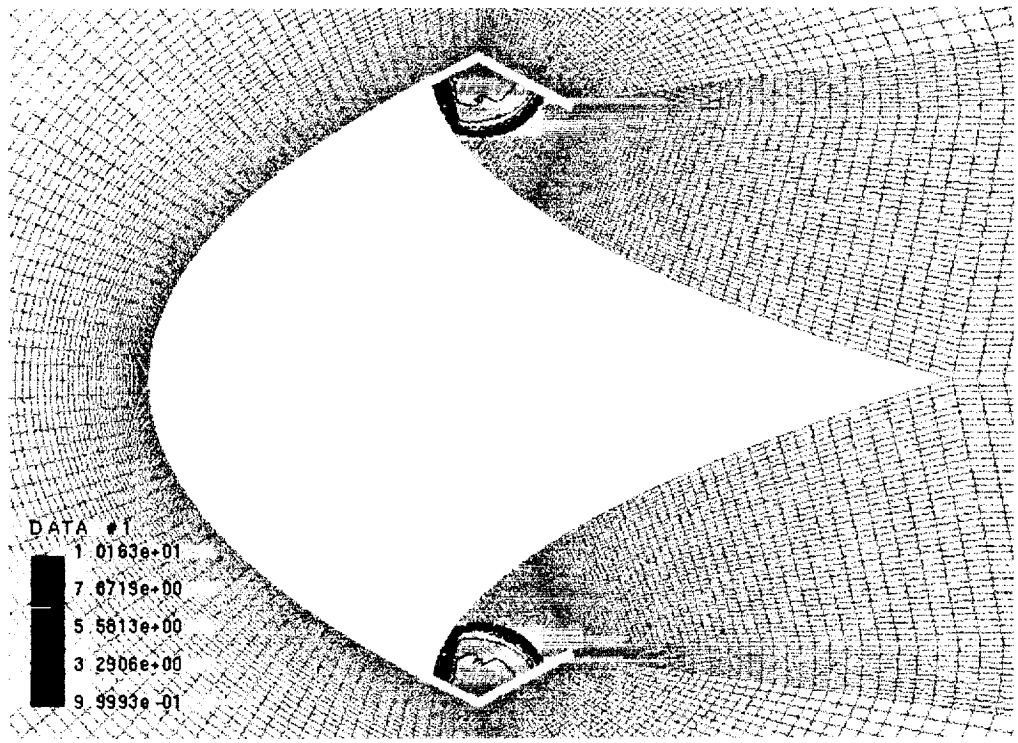

Figure 13. Pressure distributions (ATM) at 19 microseconds.

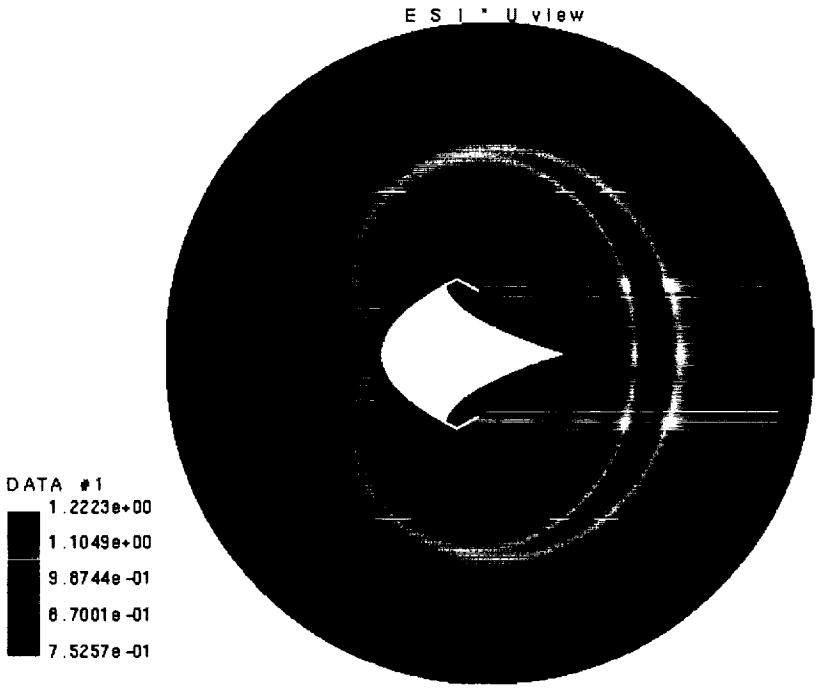

Figure 14. Pressure distributions (ATM) at 420 microseconds.

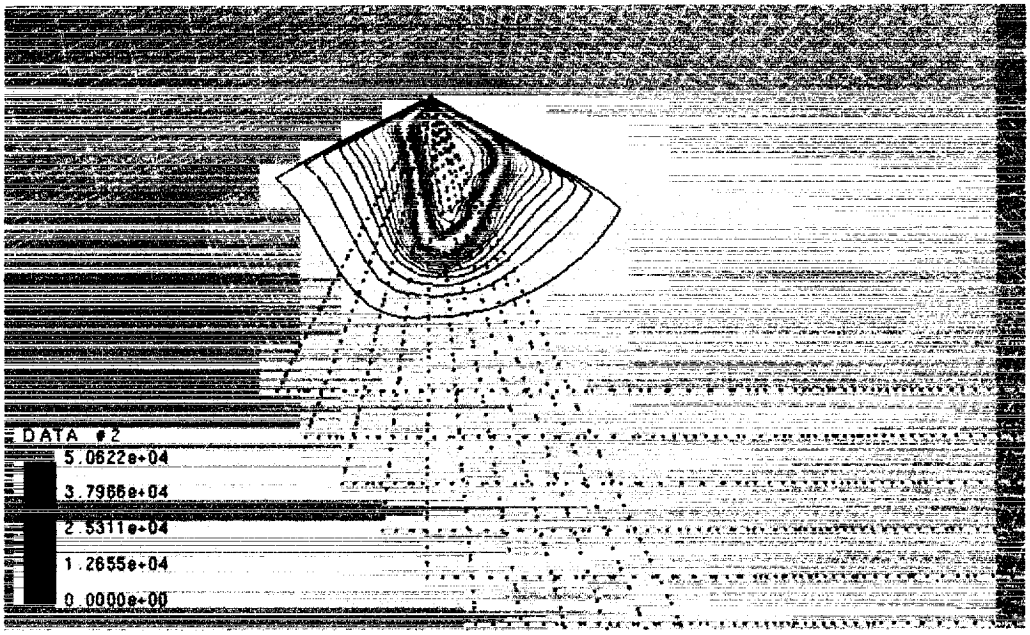

Figure 15. Temperature distributions (deg-K) at 19 microseconds without plasma frequency limit on the laser absorption.

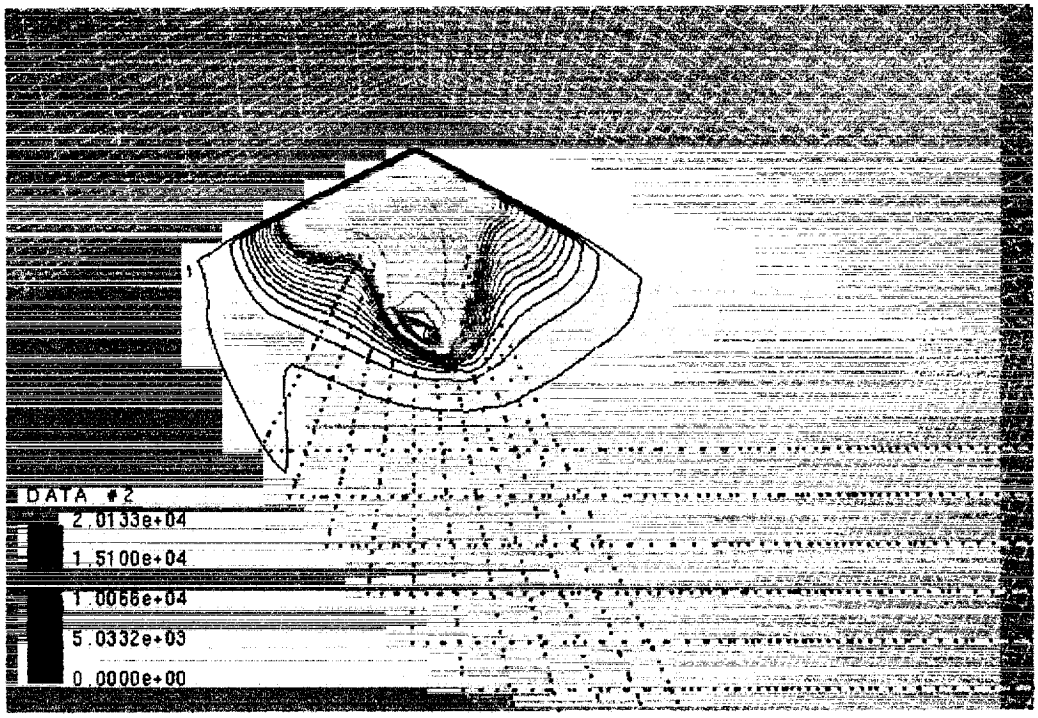

Figure 16. Temperature distributions (deg-K) at 19 microseconds with plasma frequency limit on the laser absorption.

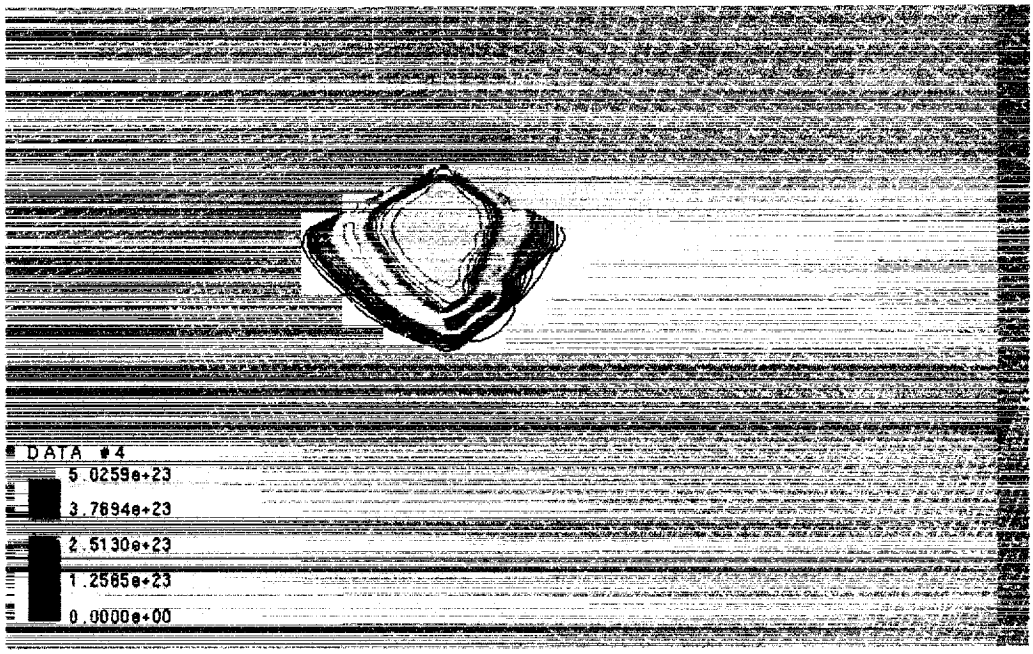

Figure 17. Electron number density distributions ($1/m^3$) at 19 microseconds.

5.3 Performance Data Comparisons

The integrated coupling coefficient curves shown in Figure 18 reveal a typical initial rise due to the pressure waves acting on the vehicle surface. After 0.00017 seconds, the coupling coefficients start to decrease due to the low pressure formed inside the cavity of the vehicle. Steady-state values of the coupling coefficients are obtained at around 0.0011 second. For each case, the steady-state coupling coefficient is obtained in 2500 time steps. Figure 18 shows that the predicted steady-state coupling coefficients for the 400, 600 and 800 Joules power level cases are 13.8, 14.5 and 14.7 dyne-sec/Joules, respectively. These results are very close to the measured data of 12.6 dyne-sec/Joules. The data comparisons would have been better if the plasma radiation model is employed in the computation. However, it would take considerably large amount of CPU time to calculate just one case. Better scheme is needed to improve the computational efficiency of the plasma radiation model such that it can be included in the present analysis.

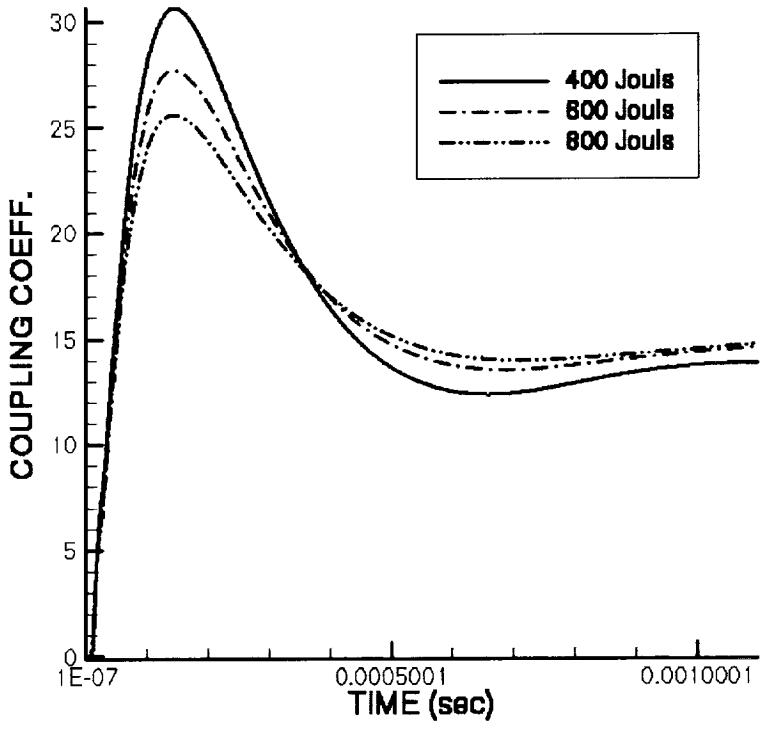

Figure 18. Predicted coupling coefficient of the model A laser lightcraft.

6. CONCLUSIONS

In the present project, a computational model has been developed for the prediction of laser propelled lightcraft performance. The present model involves the coupling of a time-accurate unstructured computational fluid dynamics (CFD) model and a robust radiative heat transfer model. Finite-rate chemistry model with high-temperature gas thermodynamics property is employed in the CFD code, UNIC-UNS. Electron and vibrational temperatures are also calculated in the present version of UNIC-UNS. Air chemistry system with 11 species and 51 reactions is used in the present analysis.

The present radiation model involves a ray-tracing model with a modified discrete transfer method for laser beam energy-absorption, propagation, reflection and focusing simulations. The modeling effort has also been spent on the investigation of the effects of high-temperature plasma radiation on the predicted plasma characteristics. It is found that the plasma radiation model does not have a major effect on the predicted strength of the detonation wave. However, it takes considerable amount of computer time to produce an answer. Therefore, the plasma radiation model is not included in the final performance data calculations.

Data comparisons of the predicted coupling coefficients for different power level have revealed good correlation with the measured data. The success of the present model is attributed to the models incorporated that reflect the physical processes occurred during the initial phase of the laser pulse. This directly affects the strength of the detonation waves that is formed through converting the laser energy to thermal energy. The faster this process occurs the stronger pressure it produces and thus higher thrust of the vehicle. Another limiting factor is the resonance of the plasma frequency with the laser frequency. This controls the duration that the laser beam can be focused effectively for thrust generation.

7. REFERENCES

1. Shang, H.M., Shih, M.H., Chen, Y.S., and Liaw, P., "Flow Calculation on Unstructured Grids with a Pressure-Based Method," Proc. of Int. Sym. on CFD, Lake Tahoe, NV, Sept. 4-8, 1995.
2. Gordon, Sanford and McBride, Bonnie J., "Computer Program for Calculation of Complex Chemical Equilibrium Compositions and Applications," NASA Reference Publication 1311, Part I: Analysis, Oct. 1994, and Part II: User's Manual and Program Description, 1996.
3. Mertogul, Ayhan Ergun, "Modeling and Experimental Measurements of Laser Sustained Hydrogen Plasmas," Ph.D. Dissertation, Mechanical Engineering, University of Illinois at Urbana-Champaign, 1993.
4. Park, Chul, "Review of Chemical-Kinetic Problems of Future NASA Missions, I: Earth Entries," J. of Thermophysics and Heat Transfer, Vol. 7, No. 3, July-Sept. 1993.
5. Chambers, L.H., "Predicting Radiative Heat Transfer in Thermochemical Nonequilibrium Flow Fields – Theory and User's Manual for the LORAN Code," NASA Technical Memorandum 4564, Sept. 1994.
6. Laux, C.O., Yu, L., Packan, D.M., Gessman, R.J., Pierrot, L. and Kruger, C.H., "Ionization Mechanisms in Two-Temperature Air Plasmas," AIAA Paper 99-3476, 30th Plasmadynamics and Lasers Conference, 28 June – 1 July, 1999, Norfolk, VA.
7. Park, Chul, "Nonequilibrium Air Radiation Program: User's Manual," NASA TM-86707, 1985.
8. Hartung, Lin, "Theory and User's Manual for Loran Code," NASA TM-4564, 1994.
9. Olynick, D. R., Henline, W. D., Chambers, L. H., and Candler, G. V., "Comparison of Coupled Radiative Flow Solutions with Project Fire II Flight Data," J. Thermophysics & Heat Transfer.
10. Anderson, J. D., "Hypersonic and High Temperature Gas Dynamics," McGraw-Hill, 1989, pp. 669.
11. Myrabo, L.N., Messitt, D.G. and Mead, F.B., "Ground and Flight Tests of a Laser Propelled Vehicle," AIAA 98-1001, 36th Aerospace Sciences Meeting & Exhibit, January 12-15, 1998, Reno, NV.

REPORT DOCUMENTATION PAGE

Form Approved
OMB No. 0704-0188

1. AGENCY USE ONLY *(Leave blank)*	2. REPORT DATE	3. REPORT TYPE AND DATES COVERED
	March 2, 2000	Final Technical Report; 3/1999 - 2/2000

4. TITLE AND SUBTITLE
LASER LIGHTCRAFT PERFORMANCE

5. FUNDING NUMBERS
H-30951D

6. AUTHOR(S)
Yen-Sen Chen, Jiwen Liu and Hong Wei

7. PERFORMING ORGANIZATION NAME(S) AND ADDRESS(ES)
Engineering Sciences, Inc.
1900 Golf Road, Suite D
Huntsville, AL 35802

8. PERFORMING ORGANIZATION REPORT NUMBER

9. SPONSORING/MONITORING AGENCY NAME(S) AND ADDRESS(ES)
George C. Marshall Space Flight Center
Marshall Space Flight Center, AL 35812

10. SPONSORING/MONITORING AGENCY REPORT NUMBER

11. SUPPLEMENTARY NOTES
Ten-See Wang / Technical Monitor

12a. DISTRIBUTION/AVAILABILITY STATEMENT

12b. DISTRIBUTION CODE

13. ABSTRACT *(Maximum 200 words)*

The purpose of this study is to establish the technical ground for modeling the physics of laser powered pulse detonation phenomenon. The principle of the laser power propulsion is that when high-powered laser is focused at a small area near the surface of a thruster, the intense energy causes the electrical breakdown of the working fluid (e.g. air) and forming high speed plasma (known as the inverse Bremsstrahlung, IB, effect). The intense heat and high pressure created in the plasma consequently causes the surrounding to heat up and expand until the thrust producing shock waves are formed. This complex process of gas ionization, increase in radiation absorption and the forming of plasma and shock waves will be investigated in the development of the present numerical model. In the first phase of this study, laser light focusing, radiation absorption and shock wave propagation over the entire pulsed cycle are modeled. The model geometry and test conditions of known benchmark experiments such as those in Myrabo's experiment will be employed in the numerical model validation simulations. The calculated performance data will be compared to the test data.

14. SUBJECT TERMS	15. NUMBER OF PAGES
Laser Propulsion, Detonation Wave Engine, Lightcraft	36
	16. PRICE CODE

17. SECURITY CLASSIFICATION OF REPORT	18. SECURITY CLASSIFICATION OF THIS PAGE	19. SECURITY CLASSIFICATION OF ABSTRACT	20. LIMITATION OF ABSTRACT
unclassified	unclassified	unclassified	unlimited